Equilibration of Circumpolar Currents with and without Topography

Ryan Abernathey * and Paola Cessi

Scripps Institution of Oceanography, La Jolla, California

ABSTRACT

The processes that determine the depth of the Southern Ocean thermocline are considered. From the perspective of heat transport, the thermocline depth is determined by the efficiency of the geostrophic circulation at transporting heat poleward. Existing conceptual frameworks focus on the importance of transient eddies, assuming that standing eddies can be neglected through transformation to a "streamwise" coordinate. Using numerical simulations of a simple circumpolar channel, we show that, when topography is present, standing eddies are the primary mechanism of poleward heat transport by the geostrophic circulation. The standing eddies are more efficient at transporting heat than the transient eddies, meaning that a flat-bottomed experiment with identical forcing has a significantly deeper thermocline. The standing eddies are also fundamentally different from transient eddies because they are not adiabatic, i.e. their heat flux is not directed along zonal-mean isotherms but rather has a significant down-gradient component. Analysis of the variance budget shows that this down-gradient transport by standing eddies is in fact sustained by a term related to the transient eddy heat flux. Thus the transient eddies remain important for the equilibration, but play a different role. A simple quasigeostrophic analytical model of a standing eddy is developed which reproduces many characteristics of the numerical solutions. The numerical model is also analyzed in streamwise coordinates; from this viewpoint, the heat balance with topography more resembles the flat-bottomed case, in which transient eddies dominate the geostrophic heat transport across the front. However, unlike the zonally symmetric flat-bottomed case, the transient eddy fluxes are highly localized downstream of topography.

1. Introduction

Mid-latitude gyre flows, confined within closed basins, produce relatively shallow stratification. In contrast, the Southern Ocean's unique geometry permits the Antarctic Circumpolar Current (ACC) to circumnavigate the globe, accompanied by much deeper stratification. The deep stratification is necessary for the thermal wind balance of such a strong baroclinic current and is intimately linked to the meridional overturning circulation (MOC). Many studies have shown that the stratification generated in the ACC pervades the global ocean below roughly 500 m depth (Toggweiler and Samuels 1995; **?**; Wolfe and Cessi 2010; Nikurashin and Vallis 2012; Munday et al. 2012). Therefore, to understand the global deep stratification and MOC, it is necessary to understand how the ACC stratification itself is determined and how this equilibrium responds to changes in forcing. There is ample evidence that the wind stress forcing the Southern Ocean has increased over decadal time scales (Marshall 2003; Toggweiler 2009) and may have been drastically reduced during the last glacial maximum (Toggweiler and Russell 2008). The means that the equilibration of the Southern Ocean is an issue of relevance for a wide range of climate problems.

The dominant paradigm for understanding the ACC stratification involves a balance between wind-driven upwelling, which tends to tilt up the isopycnals and deepen the stratification, and transient eddies produced by baroclinic instability, which work to reduce the isopycnal slope (Karsten et al. 2002). These two processes reflect the mean and eddy-driven components of the MOC. Seen from this perspective, the ACC is a version of the classic problem of macroturbulent baroclinic equilibration, similar to the midlatitude atmosphere (Green 1970; Stone 1972; Johnson and Bryden 1989; Schneider 2006; Jansen and Ferrari 2012). An increase in wind-driven upwelling can be partially or completely offset by an increase in eddy-driven restratification, resulting in an insensitivity of the ACC stratification and transport to wind changes; this behavior has been dubbed "eddy saturation" (Straub 1993; Hallberg and Gnanadesikan 2006; **?**; Viebahn and Eden 2010; Farneti et al. 2010; Abernathey et al. 2011; Meredith et al. 2012; Morrison and Hogg 2012; Munday et al. 2012).

In addition to the transient, turbulent eddy field that arises from baroclinic instability, the ACC contains many "standing eddies," steady-state meanders of the current caused by interaction with topographic features such as, for instance, the Kerguelen plateau or the Scotia Arc. There are somewhat conflicting views regarding the importance of

standing eddies in the Southern Ocean. On one hand, when the zonally-averaged fluxes due to transient and standing eddies are decomposed separately, it is clear that the standing component dominates in both idealized models with simple topography (**????**) and in realistic eddy-permitting models (Marshall et al. 1993; Karoly et al. 1997; Olbers and Ivchenko 2001; Lee and Coward 2003; **?**; **?**; Dufour et al. 2012). Inspired by the observation of de Szoeke and Levine (1981) that the mean geostrophic flow of the ACC does not transport heat across a contour of depth-averaged temperature, many authors have advocated thinking about the ACC in a "streamwise" coordinate, in order to remove the standing eddy component and emphasize importance of transient eddies (Marshall et al. 1993; Olbers et al. 2004). This streamwise-averaged perspective underpins the contemporary theoretical model of the ACC (Marshall and Radko 2003; Olbers and Visbeck 2005). Neverthless, in practice, many of the latest models continue to be analyzed using a simple zonal average (Hallberg and Gnanadesikan 2006; **?**; **?**; **?**; **?**; **?**; **?**; **?**; **?**), rather than a streamwise average, leading to a profound disconnect with the theory. (Notable exceptions are **?** and Viebahn and Eden (2012).) It is striking that even the original proponents of the streamwise coordinate (Marshall et al. 1993) declined to analyze their numerical results in this framework due to the practical difficulty, opting instead for a standard zonal average. As a result, the role of standing eddies in the eddy saturation phenomenon remains unclear.

Our study seeks to gauge the importance of standing eddies by comparing the equilibration of model ACCs with and without topography, focusing on the thermocline depth at the northern boundary as a metric of stratification. Our simulations clearly show that, in the the presence of the ridge, the stratification is significantly shallower. The thermocline always remains well above the ridge crest, so this is not a direct effect of the intrusion of topography, but rather a result of the strong southward heat transport by the standing wave. Furthermore, the stratification in the channel with a ridge displays even weaker sensitivity to wind changes; the saturation is more complete. This indicates that standing eddies are more efficient at restratifying the channel than transient eddies alone.

The time-mean flow in the ridge experiment is characterized by a large scale meander which we call the "standing wave." We perform detailed diagnostics of this standing wave, which reveal several interesting aspects. The standing wave heat flux is far from adiabatic—it has a strong component across the zonal-mean isotherms, in contrast to the transient eddy heat flux in the flat-bottomed case. To explain this behavior, we derive a temperature variance budget for the standing wave. This budget includes a term proportional to the transient-eddy heat flux convergence, which turns out to be the dominant driver of the meridional heat transport by the standing wave. We develop a quasi-linear analytical model for the standing wave that parameterizes this term as a simple Rayleigh damping of the wave temperature anomaly. Despite many simplifications, this model shows good qualitative agreement with the numerical solutions and provides valuable insight into the standing-wave dynamics.

As a final step, we analyze the heat budget in streamwise coordinates. We use two different definitions of the streamwise coordinate: the depth-integrated temperature and the barotropic transport streamfunction. The results are the same in both cases: the standing eddy flux across these contours nearly vanishes, and the transient eddies instead dominate the heat transport by the geostrophic flow. However, in contrast the the flat-bottomed case, the transient eddy heat fluxes are highly localized downstream of the topography, in a region of high eddy energy and strong gradients. This results in an overall more efficient cross-stream heat transport by the transient eddies compared with the flat-bottomed case. By diagnosing a local eddy efficiency parameter (related to an eddy diffusivity), we highlight the importance of the high-mixing region downstream of the ridge.

Throughout the paper, we frame our discussion in terms of meridional heat transport. But we note that the meridional heat transport is directly related to the vertical flux of momentum by eddies, i.e. the interfacial form stress, which is so important for the momentum balance of the ACC (Johnson and Bryden 1989; Marshall et al. 1993; Hughes 1997; Olbers 1998). One advantage of working with heat transport is that is can be integrated vertically, allowing us to easily compare the contributions of different parts of the flow. But our results regarding the relative importance of standing and transient eddies in the heat balance carry over to the momentum balance as well. *[[Here would be a good place for a discussion of Matt Mazzloff's new paper, in which standing eddies in the surface layer support a mean pressure gradient that is very important in the momentum balance.]]*

Our paper is organized as follows. Section 2 describes the model setup and experiment design. Section 3 defines a framework for characterizing the efficiency of restratification by standing and transient eddies and then applies this framework to diagnose the simulations. Section 4 contains the detailed diagnostics of the standing wave in a reference simulation. In Section 5, we present the quasi-linear analytical model of the standing wave. Analysis of the heat transport in streamwise coordiantes is conained in Section 6. Finally, discussion of the results and conclusions are given in Section 7.

2. Numerical Model Experiments

The goal of our study is investigate the relative importance of transient and standing eddies in a simple way in

order to reveal the underlying physics. The key ingredients of our model are (1) a zonally-reentrant domain, which allows a zonal current to develop; (2) westerly wind stress forcing, which drives an Eulerian-mean overturning; (3) surface buoyancy restoring, which maintains a meridional buoyancy gradient; and (4) a topographic obstruction in the abyss. We work in the adiabatic regime, with interior diapycnal mixing as weak as numerics will permit, and we use a linear equation of state with no salinity. While this setup is highly idealized, the relatively fine resolution (5 km) resolves the mesoscale eddy field well.

Following Marshall and Radko (2003), our assumption is that the first-order buoyancy balance in the ACC is between wind-driven advection by the Ekman circulation and eddy-induced advection, and that this balance determines the stratification. A second-order balance exists between the residual overturning circulation and diabatic processes, such as air-sea exchange, interior diapycnal mixing, and exchange with basins to the north. By supressing diapycnal mixing and not representing the connection to other basins, our model ACC approaches the limit of zero residual circulation described by Johnson and Bryden (1989) or Kuo et al. (2005). This means our model is appropriate for studying the first-order problem of the stratification, but not the second-order problem of the residual circulation.

The model grid and numerical parameters are nearly identical to those described in Abernathey et al. (2011), to which the reader is referred for further details. The code solves the hydrostatic, primitive, Boussinesq equations in Cartesian coordinates using the MITgcm (Marshall et al. 1997a,b). The domain is a box $L_x = 2000$ km x $L_y = 2000$ km x $H = 2985$ m. The wind stress forcing is a zonally-symmetric sinusoidal westerly jet of maximum strength τ_0 in the center of the domain, such that $\tau = \tau_0 \sin(\pi y/L_y)$. For the reference simulations, $\tau_0 = 0.2$ N m^{-2}.

The model's potential temperature equation can be written as

$$\theta_t + \boldsymbol{u} \cdot \nabla\theta = \kappa_h \nabla_h^2 \theta + (\kappa_v \theta_z)_z - \frac{\lambda}{\delta}(\theta_s - \theta^*) \ . \quad (1)$$

Here κ_h is a spatially uniform horizontal diffusivity and κ_v is a vertical diffusivity. Advection is performed using a second-order-moment scheme (Prather 1986). Explicit diffusivity (κ_h and κ_v) is set to zero, and a detailed analysis has shown that the effective numerical diapycnal diffusivity in this model is weaker than 10^{-5} m^2 s^{-1}, meaning the interior is highly adiabatic (Hill et al. 2012). However, the KPP scheme (Large et al. 1994) is employed to simulate the surface mixed layer, where κ_v is greatly enhanced. The final term represents the surface forcing, active only in the top model level; λ is a temperature relaxation inverse timescale, and δ is the thickness of the top grid cell. The surface temperature θ_s is relaxed to a linear function of latitude of the form $\theta^* = \Delta\theta(y/L_y)$. The minimum temperature is 0°C, and we choose a maximum temperature $\Delta\theta = 8$°C. This leads to a maximum buoyancy contrast of $\Delta b = g\alpha\Delta T = 1.6 \times 10^{-2}$ m s^{-2}. The relaxation timescale λ^{-1} is chosen to be 30 days (Haney 1971), which keeps the actual surface temperature very close to the prescribed profile.

In simulations with topography, a gaussian-shaped ridge is present in the middle of the domain. The motivation for this form was to capture the large meridional obstructions encountered by the ACC along is path, such as Kerguelen Plateau or the Scotia Arc. The depth in this case is given by

$$-H + h_0 e^{-x^2/\sigma^2} \ . \quad (2)$$

We selected $h_0 = 1000$ m, about one third of the total depth, and $\sigma = 75$ km, leading to a steep ridge. However, the topographic length scale σ is still large compared to the deformation radius which is approx. 15 km in the middle of the domain. Different topographic geometries can lead to different types of standing waves (**?**), but we did not explore other forms, focusing instead on the gross differences with and without topography.

The model equilibrates after about 100 years of spinup. Snapshots of the temperature field from the equilibrated state are show in Fig. 1. The time-mean isotherms are also superimposed. While both simulations contain mesoscale eddies, the figure illustrates how the flat-bottomed case is statistically symmetric in x, while the ridge case contains a standing wave in the time-mean $\overline{\theta}$ field.

3. Eddy Saturation and the Meridional Heat Transport

The mean meridional heat transport (MHT) across a latitude circle is given, in the Boussinesq approximation, by

$$\mathcal{H} = \rho_0 c_p L_x \int_{-H}^{0} \langle v(\theta - \theta_0) \rangle dz \quad (3)$$

where ρ_0 and c_p are, respectively, the reference density and specific heat of seawater, v is the meridional velocity, θ is the potential temperature, and the angle brackets indicate a zonal and time average (**?**). Since the total vertically-integrated mass flux across a latitude circle (or any other circumpolar contour) must vanish, an arbitrary constant θ_0 can be chosen without changing $\mathcal{H}$ (de Szoeke and Levine 1981). By choosing this constant to be the temperature of the abyss, 0° C, we can allow ourselves to ignore the contribution to the heat transport by the deep mean flows, such as the bottom Ekman flow or the geostrophic flow below topography, in which $\theta \simeq \theta_0$.

In the adiabatic limit, $\mathcal{H}$ must tend to zero in a model such as ours. This is because any nonzero $\mathcal{H}$ must be balanced by an air-sea heat flux. But since the residual circulation also tends to zero, there is no advective term to balance such an air-sea flux at the surface (Marshall and

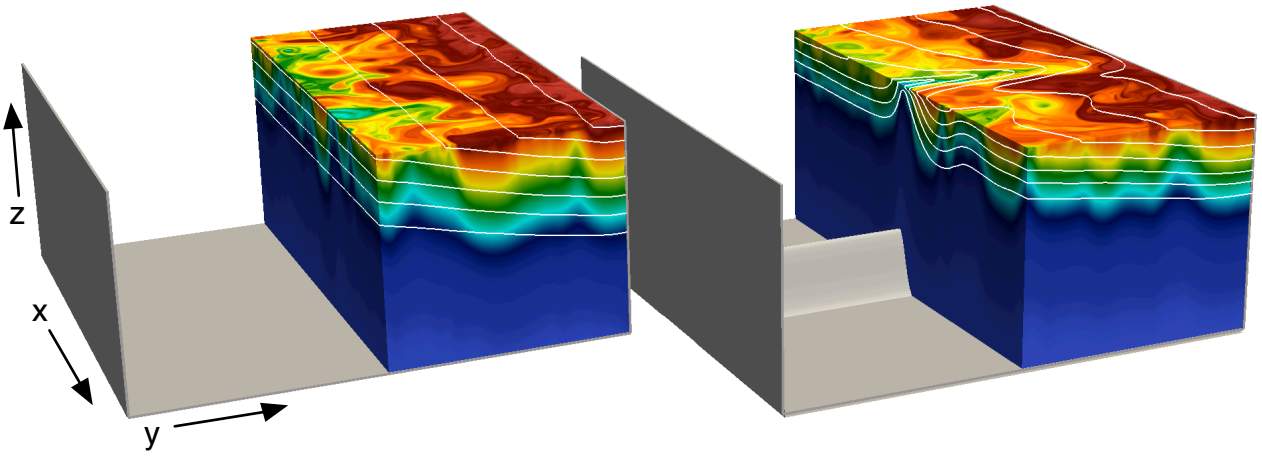

FIG. 1. Colors show an instantaneous snapshot of the θ field from each reference experiment (flat on the left, ridge on the right). The color scale ranges from 0 to 8°C. The field has been clipped at $y = 1000$ km, the meridional midpoint, to reveal a zonal cross section. The white contours are the time-mean isotherms $\overline{\theta}$, illustrating the statistical zonal symmetry of the flat-bottomed case and the standing wave in the ridge.

Radko 2003). In practice, we do not achieve a truly vanishing MOC or MHT due to diabatic effects in the surface layer. Our model contains a weak overturning cell in the top 200 m, similar to the one noted by Kuo et al. (2005). However, this is clearly a second-order effect, and as the subsequent analysis shows, we remain very close to the limit of zero net MHT. This vanishing-residual MOC limit is a useful idealization of the real ACC, in which there is a nonzero MHT and MOC, but where large cancellations between mean and eddies nevertheless occur (Speer et al. 2000; Hallberg and Gnanadesikan 2006; **?**).

We can use this constraint on the heat transport to derive a scaling for the termocline depth. Thanks to our choice of θ_0, the heat transported by the mean overturning circulation is simply the heat transported in the Ekman layer:

$$\mathcal{H}_{Ek} = \rho_0 c_p L_x V_{Ek} \langle \theta_s \rangle \sim -c_p L_x \frac{\tau}{f} \Delta\theta \frac{y}{L_y} \ . \tag{4}$$

This is an equatorward heat transport which is determined solely by externally specified parameters. Then there is a heat transport by the geostrophic flow:

$$\mathcal{H}_g = \rho_0 c_p L_x \int_{-h}^{0} \langle v_g \theta \rangle dz \ . \tag{5}$$

This heat transport occurs over the thermocline of depth h, below which $\theta = 0$. Because there is no zonal pressure gradient above the topography, $\langle v_g \rangle = 0$, meaning that $\mathcal{H}_g$ arrises only from eddy correlations; it potentially contains contributions from both standing and transient eddies.

In order to maintain the heat balance, the geostrophic motions in the interior must transport heat poleward at the same rate as the Ekman circulation transports it equatorward. Setting $\mathcal{H} = \mathcal{H}_{Ek} + \mathcal{H}_g \approx 0$.

A scaling can be derived based on residual mean theory, following Karsten et al. (2002). The Eulerian-mean overturning cell, whose strength is determined by the wind-driven Ekman transport, is $\langle \psi \rangle = -tau/(\rho_0 f)$. We express the eddy-induced circulation as $\psi^* = \langle v_g \theta \rangle / \langle \theta_z \rangle$. The vanishing residual circulation requires

$$0 = \langle \psi \rangle + \psi^* = -\frac{\tau}{\rho_0 f} + \frac{\langle v_g \theta \rangle}{\langle \theta_z \rangle} \ . \tag{6}$$

Because all the temperature classes are supplied at the surface, we have $\langle \theta_z \rangle \sim \Delta\theta / h$, where h is the scale of the thermocline depth h. Using the vanishing of the residual circulation we arrive at the scaling

$$h = \frac{\tau_0 \Delta\theta}{\rho_0 f \langle v_g \theta \rangle} \tag{7}$$

The sensitivity of the thermocline depth h to wind changes depends on the heat transport by geostrophic motions. If $\langle v_g \theta \rangle$ is approximately independent of the wind stress, the thermocline depth scales linearly with τ_0. The concept of "eddy saturation," in which h becomes independent of τ_0, implies that $\langle v_g \theta \rangle \propto \tau_0$. In general $\langle v_g \theta \rangle$ exhibits a dependence on τ_0 that is intermediate between these two limits (Spence et al. 2009; Meredith et al. 2012). Here we contrast the sensitivity of $\langle v_g \theta \rangle$ and h to τ_0 with and without topography, finding a higher level of "saturation", i.e. a smaller sensitivity of h on the wind stress.

As a practical matter, we find h via the expression

$$h = 2 \frac{\int_{-H}^{0} z \langle \theta \rangle dz}{\int_{-H}^{0} \langle \theta \rangle dz} \tag{8}$$

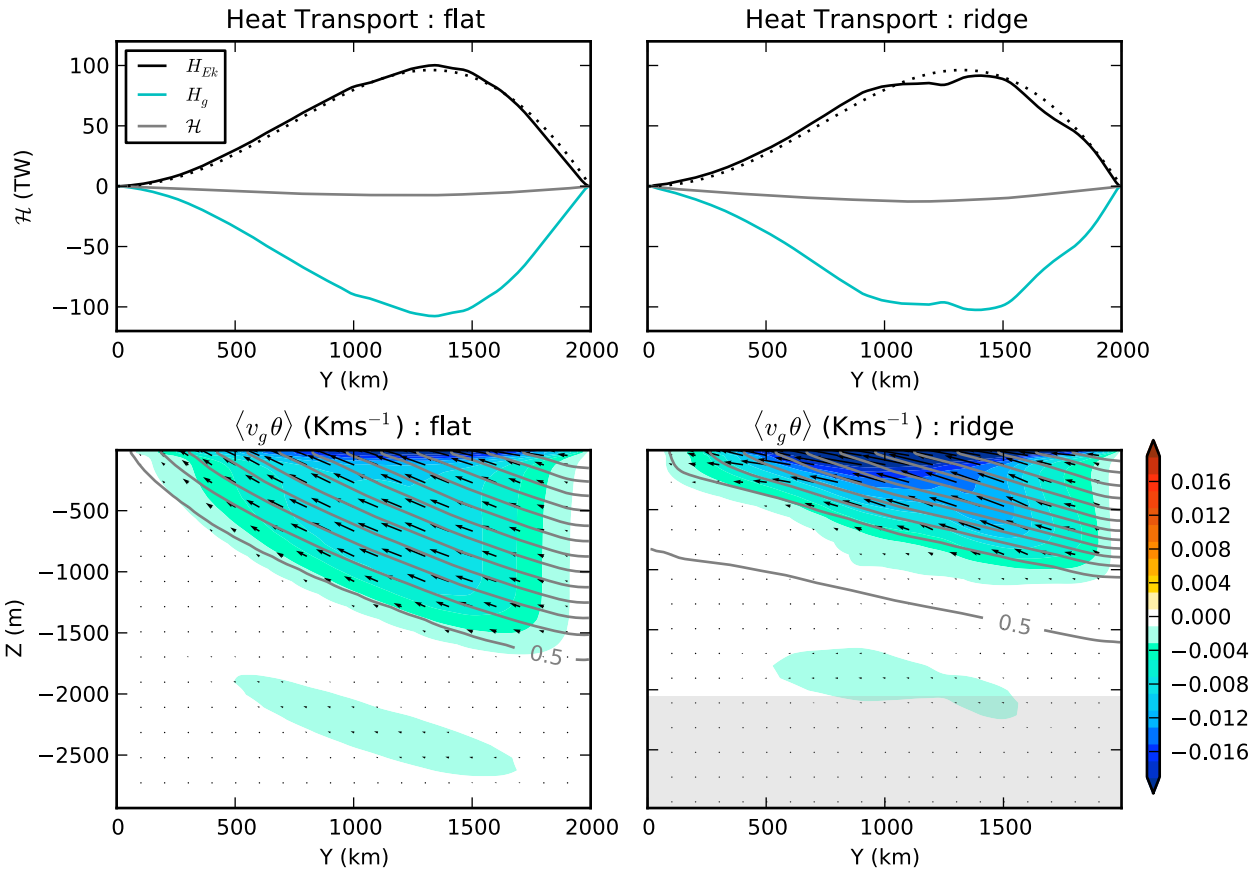

FIG. 2. *Top panel:* the meridional heat transport, $\mathcal{H} = \mathcal{H}_{Ek} + \mathcal{H}_g$, from the same experiments. The black dotted line is the approximate form of $\mathcal{H}_{Ek}$ from the RHS of (4). $\mathcal{H}_g$ is just the vertical integral of the bottom panel. *Bottom panel:* zonal and time-mean temperature flux by the geostrophic flow $\langle v_g\theta\rangle$ in color. The black arrows indicate the direction the flux in the (y, z) plane and the grey contours show the zonal mean isotherms $\langle\theta\rangle$, contoured every $0.5°C$. The shaded area in the lower right panel shows the height of the topographic ridge.

evaluated at the northern boundary, where the thermocline is deepest. This is a standard method for characterizing thermocline depth (**???**).

To illustrate these concepts, we present diagnostics of $\langle v_g\theta\rangle$ and $\mathcal{H}$ in Fig. 2. This figure compares the reference simulations ($\tau_0 = 0.2$ N m^{-2}) with and without the topographic ridge. The upper panel demonstrates that $\mathcal{H}_{Ek}$ and $\mathcal{H}_g$ are essentially the same in both cases, with $\mathcal{H}_{Ek}$ remaining very close to the approximation defined in (4). $\mathcal{H}_g$ compensates almost completely for $\mathcal{H}_{Ek}$, meaning that $\mathcal{H}$, the net MHT, remains very close to zero. The difference between the two simulations is only revealed when the bottom panel is examined; the heat transport in the ridge case is confined to a shallower layer, implying a smaller value of h, i.e. a shallower thermocline. Specifically, according to (8), the thermocline depth at the northern boundary is approx. 1200 m in the flat-bottom experiment and 1000 m in the ridge experiment. Lest this difference seem small, we note that it leads to a *doubling* of the thermal-wind induced circumpolar volume transport. This transport is given by

$$T = -\frac{g\alpha}{f}\int_0^{Ly}\int_{-2000\text{ m}}^{0}\frac{\partial\langle\theta\rangle}{\partial y}dzdy\ . \tag{9}$$

(We integrate only above 2000 m, the depth of the ridge crest, to fairly compare both experiments.) The value of T is 55 Sv in the ridge case and 107 Sv in the flat case. Because $\langle\theta\rangle_y$ remains fixed at the surface, thermal wind implies that $T \propto h^2$.[1]

[1]It is important to note that, in the flat-bottom case there is also a very strong barotropic component of the zonal transport that is frictionally balanced (Cessi 2007; Abernathey et al. 2011). The magnitude of this transport is directly proportional to the wind stress and inversely proportional to the linear bottom drag parameter. In

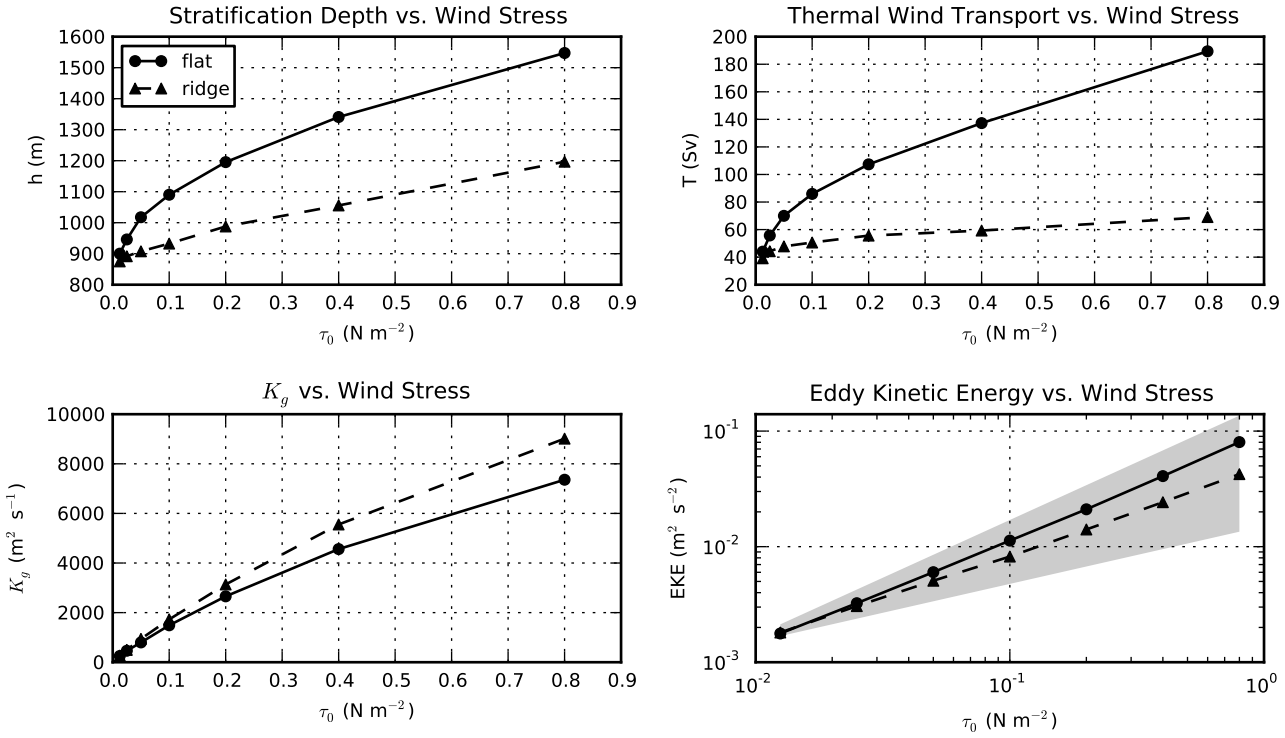

FIG. 3. Comparison of global variables in flat-bottom (circles, solid lines) and ridge (triangles, dashed lines) experiments. *Top left:* the stratification depth h at the northern boundary, evaluated from (8). *Top right:* the area integrated bottom velocity U_0. *Bottom left:* The geostrophic heat transport $\langle v_g \theta \rangle$, averaged over all latitudes. *Bottom right:* the eddy kinetic energy, plotted in log-log space. The gray envelope indicates the range of proportionality between $\tau_0^{1/2}$ and τ_0^1.

We now explore how the thermocline depth changes as a function of wind stress. We run the flat and the ridge experiments for the following values of τ_0: 0.0125, 0.025, 0.05, 0.1, 0.2, 0.4, and 0.8 N m^{-2}. This range constitutes six successive doublings of the wind stress. The values of h, U_{bottom}, and $\langle v_g \theta \rangle$ are plotted in Fig. 3. While the variables are quite close with and without topography for the weakest winds, they quickly diverge as the winds are increased. For the strongest winds, h is over 300 m deeper without the topography, while U_0 ?????. The general principle of eddy saturation is reflected in h, which shows that, as the winds increase, the geostrophic flow becomes more and more efficient at transporting heat poleward, leading to a weak dependence of h on τ_0.

Recent studies have used the domain-averaged transient eddy kinetic energy (EKE) as a proxy for the strength of the eddy-driven circulation (Meredith and Hogg 2006; Abernathey et al. 2011; Meredith et al. 2012; **?**; Munday et al. 2012). According to this argument, a model with a higher EKE will have a higher $\langle v_g \theta \rangle$ and therefore a shallower thermocline. To test this idea, we calculated the EKE in our simulations (Fig. 3). Both models have very similar EKE for weak values of τ_0. As the winds are increased, the values diverge; the EKE in the flat-bottomed model is always *higher* than the corresponding ridge case and is nearly linearly proportional to τ_0. The EKE in the model with topography displays a slightly weaker dependence on τ_0. Nevertheless, $\langle v_g \theta \rangle$ is greater with topography. This seems to upset the paradigm put forth by Meredith et al. (2012), in which the EKE dependence on winds controls the degree of eddy saturation.

This simple set of experiments demonstrates the importance of topographic effects in determining the Southern Ocean stratification. No coordinate transformation (e.g. to a streamwise coordinate system) will alter the fact that the stratification at the northern boundary is shallower when topography is present, or that the thermal-wind zonal

the reference simulations discussed here, it has a magnitude of 450 Sv, completely overwhelming the thermal-wind transport. But it is not dependent on the stratification. In the ridge case, this frictional component is mostly absent, and the bottom velocity is determined through the topographic form drag available to close the zonal momentum budget (**?**).

transport is much less. But beyond these quantitative differences, there are great qualitative differences in how the two system equilibrate. In the rest of the paper, we further explore the results from two different perspectives. From the standard zonally-averaged perspective, the clear difference is that topography generates a standing wave which is highly efficient at transporting heat poleward. In the next section, we diagnose the model from this perspective. We decompose $\mathcal{H}_g$ into transient and standing components and show that the standing component becomes increasingly dominant as the winds increase. In Sec. 6, we instead consider the "streamwise" perspective, in which standing eddy fluxes are greatly reduced. From this perspective, a highly localized region of cross-stream transient eddy heat flux downstream of the ridge is responsible for the greater overall heat transport efficiency. While Both these perspectives are formally "correct," they offer somewhat distinct views on the dynamics responsible for equilibrating the thermocline.

4. Heat Transport by the Standing Wave

a. Standing and Transient Eddies

At this point, we must carefully define conventions for time and zonal averaging. The time average of a variable $A(x, y, z, t)$ over interval ΔT is

$$\overline{A}(x, y, z) = \Delta T^{-1} \int_t^{t+\Delta T} A dt \ . \tag{10}$$

We will only take zonal averages of already time-averaged fields. Other conventions are possible (see discussion in Viebahn and Eden 2012), but this is the most informative decomposition. The zonal / time average is

$$\langle A \rangle(y, z) = \langle \overline{A} \rangle = L_x^{-1} \int_0^{L_x} \overline{A} dx \ . \tag{11}$$

We define the anomalies as follows:

$$\begin{aligned} A' &= A - \overline{A} \\ A^\dagger &= \overline{A} - \langle A \rangle \end{aligned} \tag{12}$$

such that $A = \langle A \rangle(y, z) + A^\dagger(x, y, z) + A'(x, y, z, t)$. The standing wave is associated with $A^\dagger$. In a flat-bottom simulation with statistical symmetry in the x direction, $A^\dagger = 0$.

Taking a zonal and time average of the θ equation (1), we obtain

$$\begin{aligned} \langle \boldsymbol{u} \rangle \cdot \nabla \langle \theta \rangle + \nabla \cdot \langle \boldsymbol{u}^\dagger \theta^\dagger \rangle + \nabla \cdot \langle \overline{\boldsymbol{u}' \theta'} \rangle = \\ \kappa_h \nabla_h^2 \langle \theta \rangle + (\langle \kappa_v \theta_z \rangle)_z - \frac{\lambda}{\delta} (\langle \theta \rangle_0 - \theta^*) \ . \end{aligned} \tag{13}$$

Integrating this equation once in y gives an equation for the meridional heat transport. All the diabatic terms on the RHS are quite small compared to the advective terms. To relate these advective terms to the components of the heat transport mentioned in the previous section, we note that $\langle v \rangle$ is associated with the Ekman overturning, and therefore

$$\mathcal{H}_{Ek} = \rho_0 c_p L_x \int_{-H}^0 \langle v \rangle \langle \theta \rangle dz \tag{14}$$

while $\mathcal{H}_g$ can be split into two components, one due to standing eddies ($\mathcal{H}_{SE}$) and another due to transient eddies ($\mathcal{H}_{SE}$) :

$$\begin{aligned} \mathcal{H}_g = \rho_0 c_p L_x \int_{-H}^0 (\quad & \langle v^\dagger \theta^\dagger \rangle + \langle \overline{v' \theta'} \rangle \quad) dz \\ = \quad & \mathcal{H}_{SE} + \mathcal{H}_{TE} \quad . \end{aligned} \tag{15}$$

For the flat-bottom experiments, $\mathcal{H}_{SE} = 0$.

In Fig. 4, we use this framework to decompose the MHT from Fig. 2 into standing and transient eddy contributions. This figure makes it clear that $\mathcal{H}_{SE}$ is the dominant contributor to $\mathcal{H}_g$. This result has been found whenever eddy fluxes are decomposed in this way, in a wide range of models (**????**Olbers and Ivchenko 2001; Lee and Coward 2003; **?**; **?**; Dufour et al. 2012). Nevertheless, we point it out again here because the recent literature has focused so much on the importance of *transient* eddies in eddy saturation and compensation (**??**Meredith et al. 2012; Morrison and Hogg 2012).

Fig. 4 illustrates the balance in a single experiment but does not address the response to changing winds. We now plot the $\mathcal{H}_g$, $\mathcal{H}_{SE}$ and $\mathcal{H}_{TE}$ at $y = 1250$ km (approximately where the heat transport is most intense) as a function of τ_0 for each of the experiments in Fig. 5. The figure shows that it is $\mathcal{H}_{SE}$ which responds to compensate for the increasing value of $\mathcal{H}_{Ek}$. In fact, $\mathcal{H}_{TE}$ actually *decreases* weakly with τ_0 at this latitude, becoming more and more negligible in comparison with $\mathcal{H}_{SE}$. We conclude that, when analyzed from a zonally averaged perspective, the eddy saturation is primarily a phenomenon of *standing* eddy saturation. A similar conclusion was recently reached by (Dufour et al. 2012) in the analysis of the overturning circulation of a realistic Southern Ocean model.

b. What drives the standing eddy heat transport?

It is clear why transient eddies must transport heat toward the pole. Arising from baroclinic instability of the mean state, their energy source is the available potential energy (APE) contained in the sloping isopycnals of the ACC. The transfer from APE to EKE is expressed in the eddy energy budget as a positive term $g\alpha\langle \overline{w'\theta'} \rangle$. Under statistically steady, adiabatic conditions, this vertical heat flux must be accompanied by a meridional flux $-\langle \overline{v'\theta'} \rangle \langle \theta \rangle_y = \langle \overline{w'\theta'} \rangle \langle \theta \rangle_z$, so that the heat flux is directed entirely *parallel* to the mean isotherms, with no cross-gradient component. This behavior is evident in Fig. 2 (left panel), which includes arrows showing the direction of the heat flux

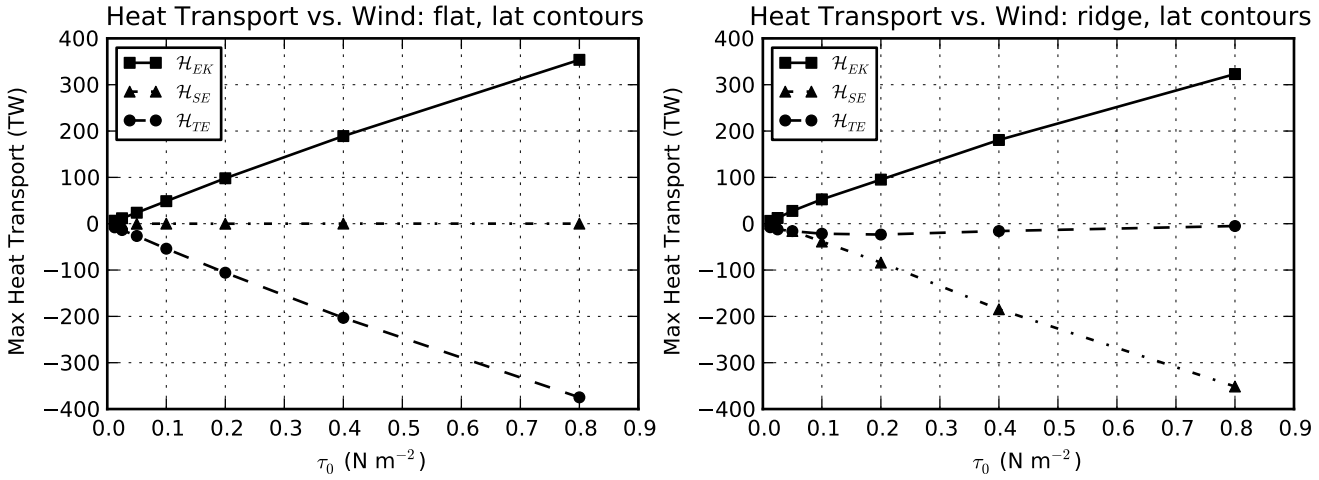

FIG. 5. The different components of the meridional heat transport across $y = 1250$ km (where $\mathcal{H}_{Ek}$ is roughly maximum) for different values of the wind stress parameter τ_0. The components are: $\mathcal{H}_{Ek}$ (solid / squares), the Ekman induced heat transport; $\mathcal{H}_{SE}$ (dash-dot / triangles), the standing eddy heat transport; and $\mathcal{H}_{TE}$ (dashed / circles), the transient eddy heat transport. The flat-bottom experiments are on the left, and the ridge experiments are on the right.

in the meridional plane; the arrows clearly point along the isotherms. Because of this energy pathway, when transient eddies are the only contributor to the MHT, it is indeed reasonable to associate increased $\mathcal{H}_g$ with higher EKE.

It is not so obvious why standing eddies should transport heat poleward. They do not arise from baroclinic instability, but rather from interactions of the current with topography. The meanders of the ACC are often explained using an "equivalent barotropic" analysis, in which the current is characterized by a single mode which decays (usually exponentially) with depth (**?**). While such models successfully explain many of the features of the ACC, they says nothing about the heat transport by standing eddies. This is because equivalent barotropic flow cannot transport any heat. Heat transport in geostrophic flow requires at least two vertical modes (**?**).

Some progress can be made by considering the standing-wave variance budget. To derive this budget, subtract (13) from (1), multiply the result by $\theta^\dagger$, and take a zonal and time average. The result,

$$\frac{\partial}{\partial t}\frac{\langle\theta^{\dagger 2}\rangle}{2} + \nabla\cdot\left(\langle\boldsymbol{u}\rangle\frac{\langle\theta^{\dagger 2}\rangle}{2} + \frac{\langle\boldsymbol{u}^\dagger\theta^{\dagger 2}\rangle}{2}\right) + \langle\boldsymbol{u}^\dagger\theta^\dagger\rangle\cdot\nabla\langle\theta\rangle = -\langle\theta^\dagger\nabla\cdot(\overline{\boldsymbol{u}'\theta'})\rangle - \kappa_h\langle|\nabla\theta^\dagger|^2\rangle - \langle\kappa_v|\theta^\dagger_z|^2\rangle - \frac{\lambda}{\delta}\langle\theta^{\dagger 2}_s\rangle\ , \tag{16}$$

where transport terms due to variance diffusion have been neglected. This equation resembles a standard tracer variance equation, except for the first term on the RHS, which describes the interaction of the standing eddies with the transient eddies.

We have diagnosed this budget from our simulations. The last three terms (mixing- and forcing-related) are negligible except for a small contribution close to the surface. This indicates that surface forcing is not important for driving the standing-wave heat transport. The mean advection term is also small. If we neglect these terms, divide by $\langle\theta\rangle_y$, and integrate in z, we find an approximate expression for what is driving the standing eddy heat transport:

$$\begin{aligned}\mathcal{H}_{SE} &= \rho_0 c_p L_x \int_{-H}^{0}\langle v^\dagger\theta^\dagger\rangle dz \\ &= -\rho_0 c_p L_x\int_{-H}^{0}\langle\theta\rangle_y^{-1}\left[\langle w^\dagger\theta^\dagger\rangle\langle\theta\rangle_z + \nabla\cdot\frac{\langle\boldsymbol{u}^\dagger\theta^{\dagger 2}\rangle}{2} + \langle\theta^\dagger\nabla\cdot(\overline{\boldsymbol{u}'\theta'}\right. \\ &= \mathcal{H}^w_{SE} + \mathcal{H}^{tc}_{SE} + \mathcal{H}^{te}_{SE}\ . \end{aligned}\tag{17}$$

The three components $\mathcal{H}^w_{SE}$, $\mathcal{H}^{tc}_{SE}$ and $\mathcal{H}^{te}_{SE}$ are associated respectively with the three terms in the second line of (17). Each represents a distinct physical process driving the standing eddy heat transport. The first $\mathcal{H}^w_{SE}$, is associated with the vertical buoyancy flux by the standing wave. The second, $\mathcal{H}^{tc}_{SE}$, is the so-called nonlinear "triple correlation" term, resulting from advection of $\theta^{\dagger 2}$ by the standing wave itself. The final one, $\mathcal{H}^{te}_{SE}$, is due to the correlation of $\theta^\dagger$ with heat flux convergence by the transient eddies. These three components are plotted in Fig. 6.

Overall the balance can be summarized as follows. There is a large degree of cancellation between $\mathcal{H}^w_{SE}$ and $\mathcal{H}^{tc}_{SE}$; that is, the variance production by the $\langle w^\dagger\theta^\dagger\rangle\langle\theta\rangle_z$ terms is largely balanced by variance transport by the triple correlation term. On the other hand, the transient-eddy related term $\mathcal{H}^{te}_{SE}$ is the dominant driver of the poleward

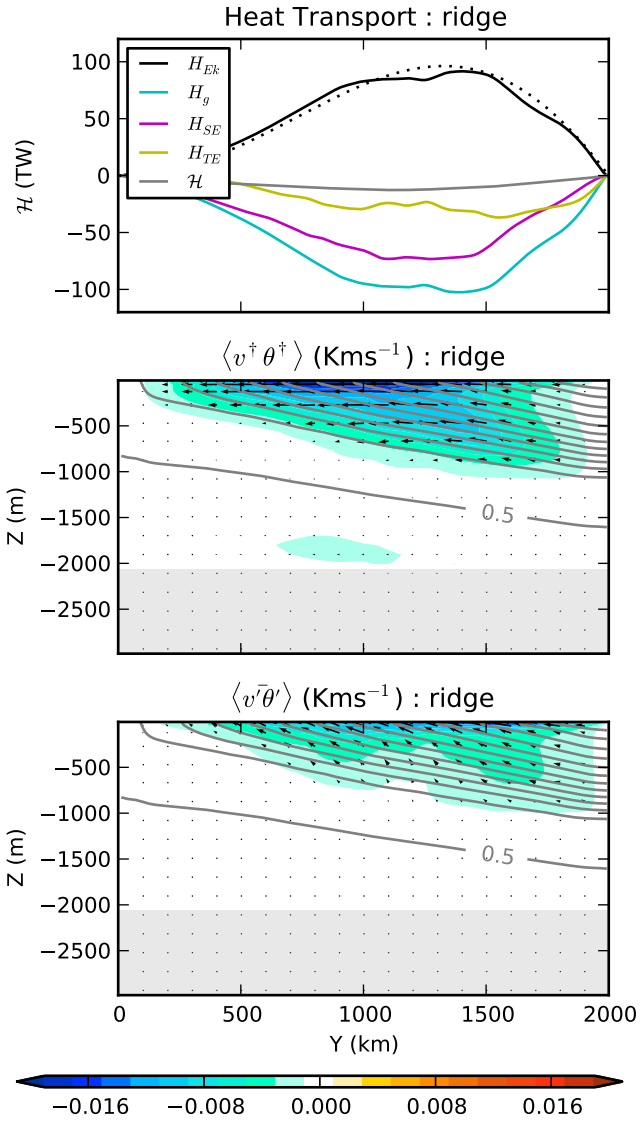

FIG. 4. *Top panel:* the meridional heat transport from the ridge experiment, with $\mathcal{H}_g$ decomposed into standing ($\mathcal{H}_{SE}$) and transient ($\mathcal{H}_{TE}$) eddy components. Otherwise the same as Fig. 2.

heat transport by the standing wave. This is an interesting result; it means that, although the transient eddies are relatively unimportant in the meridional heat transport itself, the local transient eddy heat convergence can nevertheless be crucial for the standing wave meridional heat transport.

From an energetic perspective, the balance of terms in (16) states that dominant potential energy pathway is for potential energy to come from the mean flow to the standing wave (via the term $\langle v^\dagger \theta^\dagger \rangle \partial \langle \theta \rangle / \partial y$), and then from the standing wave to the transient eddy field (via the term

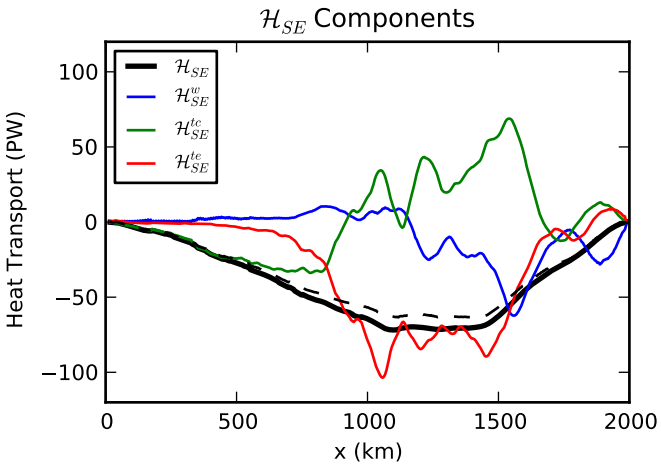

FIG. 6. In color are the three different drivers of the standing eddy heat flux $\mathcal{H}_{SE}$ defined in (17). The thick black line is the net $\mathcal{H}_{SE}$, and the thin dashed black line is the sum of the three terms $\mathcal{H}^w_{SE}$, $\mathcal{H}^{tc}_{SE}$, and $\mathcal{H}^{te}_{SE}$. The closeness of the two black lines indicates that the approximation in (17) works very well.

$\langle \theta^\dagger \nabla \cdot (\overline{\boldsymbol{u}'\theta'}) \rangle$. Most of the dissipation must therefore occur in the transient eddy part of the flow, through bottom drag.

5. Linear Quasi-geostrophic Model

In order to better understand the dynamics of the standing wave, we have developed a simple analytical model...

[[Have to decide how much of the analytical solution to include here vs appendix.]]

6. Heat Transport Across Streamlines

It has long been recognized that the importance of standing eddies is greatly reduced by adopting a coordinate system which follows the meanders of the ACC. One such coordinate system was proposed by de Szoeke and Levine (1981), who analyzed the heat transport across a contour of depth-averaged potential temperature. (We will call this quantity Θ.) While this coordinate is not precisely a streamline of the ACC, the Θ contours are certainly much more aligned with the ACC streamlines than are latitude circles. By analyzing a hydrographic atlas of the Southern Ocean, de Szoeke and Levine (1981) found that the time-mean geostrophic flow transports no heat across a Θ-contour within the ACC. They inferred that transient eddy heat transport was required to close the heat budget. This conclusions was later confirmed by performing the same analysis in numerical models, where the transient eddy flux

was known (**?**).

The idea of "streamwise" coordinates was taken up from the perspective of the momentum budget by Marshall et al. (1993). They noted that, in an isopycnal coordinate system, the standing eddy component of the interfacial form stress (related to the meridional heat transport) could be eliminated completely by averaging along time-mean contours of the Montgomery potential in each isopycnal layer. Transient eddy interfacial form stress was therefore required to close the momentum budget. Such an analysis was performed by **?** and **?** in idealized models; they both found that the transient eddy flux across Montgomery-potential contours was highly localized in regions downstream of topographic features. The notion that standing eddies can be removed by a coordinate transformation became a cornerstone of the residual-mean model of the ACC, which should be interpreted as a mean along streamlines (Karsten and Marshall 2002; Marshall and Radko 2003; Olbers et al. 2004; Olbers and Visbeck 2005). But these theoretical models were strongly influenced by laboratory and numerical experiments without topography, in which a zonal and streamwise average are indistinguishable (Karsten et al. 2002; Marshall et al. 2002; Cenedese et al. 2004; Kuo et al. 2005). One shortcoming of this analogy is that truly zonally symmetric models have uniform eddy statistics in x, while models with topography can have strong local hotspots of cross-stream eddy flux (Thompson 2010). (This is precisely what we find below.)

Most recently, Viebahn and Eden (2012) examined how to best construct the meridional overturning streamfunction using both along-isopycnal and along-streamline integration paths. The goal of this analysis was to eliminate completely the standing-eddy contribution to the MOC, which is directly related to both the heat transport and the interfacial form stress. They found that the standing-eddy component could only be eliminated completely by using a streamwise coordinate which varied with depth (similar to the conclusion by Marshall et al. 1993); since such a coordinate system would be non-orthogonal, this transformation comes at the expense of great geometrical complexity: the coordinate is not know a priori, and depends on the flow. Viebahn and Eden (2012) conclude that a streamwise coordinate which does not vary with depth (like that of de Szoeke and Levine 1981) is adequate to remove most of the standing eddies component.

One goal of streamwise averaging is to make the real ACC, with its complex meanders, as close as possible to a zonally symmetric flow. The conceptual advantages of this transformation for simple theoretical models are clear. But our experiments have shown that a zonally symmetric channel with the exact same forcing is different in important ways from one with topography. (For instance, the thermal-wind transport is halved with topography.) In the previous sections, we attributed this difference to the presence of heat transport by the standing eddies. But how can the difference be explained when the standing eddies have been eliminated through averaging along streamlines? This is the question we now take up.

a. Streamwise Coordinate Systems

The time-mean heat transport across any closed contour S_0 of $S(x,y)$ can be expressed as

$$\mathcal{H}^{S_0} = \rho_0 c_p \oint_{S_0} \left(\int_{-H}^{0} \overline{\boldsymbol{v}\theta} dz \right) \cdot \hat{\boldsymbol{n}} dS \tag{18}$$

$$= \rho_0 c_p \int\int_{S<S_0} \nabla \cdot \left(\int_{-H}^{0} \overline{\boldsymbol{v}\theta} dz \right) dx dy \tag{19}$$

where $\hat{\boldsymbol{n}} = \nabla S / |\nabla S|$ is the unit normal vector to S. The overbar indicates a time average, as in the preceding sections. In the second line, we have used the divergence theorem, yielding an expression that is much easier to evaluate in practice from a numerical model. We employ with two different streamwise coordinate systems. The first is defined by Θ, identically to de Szoeke and Levine (1981). The other uses the barotropic transport streamfunction Ψ. Formally these two quantities are defined by

$$\Theta(x,y) = \frac{1}{H} \int_{-H}^{0} \overline{\theta} dz$$

$$\Psi(x,y) = -\int_{0}^{y} \int_{-H}^{0} v dz dy' \ . \tag{20}$$

S can be either Θ or Ψ. In what follows, we refer to both these contours as "streamlines." As we will see, the results of our analysis using these two coordinates are similar in most ways. The two fields are plotted in Fig. 7. The isolines of both are primarily zonal away from the ridge but meander coherently above and downstream of the ridge. These meanders arise due to the standing-wave dynamics discussed in the preceding sections. An important qualitative *difference* between Ψ and Θ is that Ψ contains regions of closed contours that do not circumnavigate the domain (for example, the regions where $\Psi < -15$ Sv or $\Psi > 75$ Sv). The transport across these contours can no longer be interpreted as across the circumpolar current; rather, it is across the boundary of a barotropic gyre-like recirculation. On the other hand, there are certain Θ contours that are not closed at all, but intersect the northern boundary ($\Theta > 1.6°$C). Despite these problematic regions, the contours of both quantities are well-behaved over most of the domain, accurately representing the meandering front.

To isolate the physical processes governing the cross-stream heat transport, we separate the term $\overline{\boldsymbol{v}\theta}$ into ageostrophic (i.e. Ekman), standing eddy, and transient eddy components as follows:

$$\overline{\boldsymbol{v}\theta} = \overline{\boldsymbol{v}}_a \overline{\theta} + \overline{\boldsymbol{v}}_g \overline{\theta} + \overline{\boldsymbol{v}'\theta'} \tag{21}$$

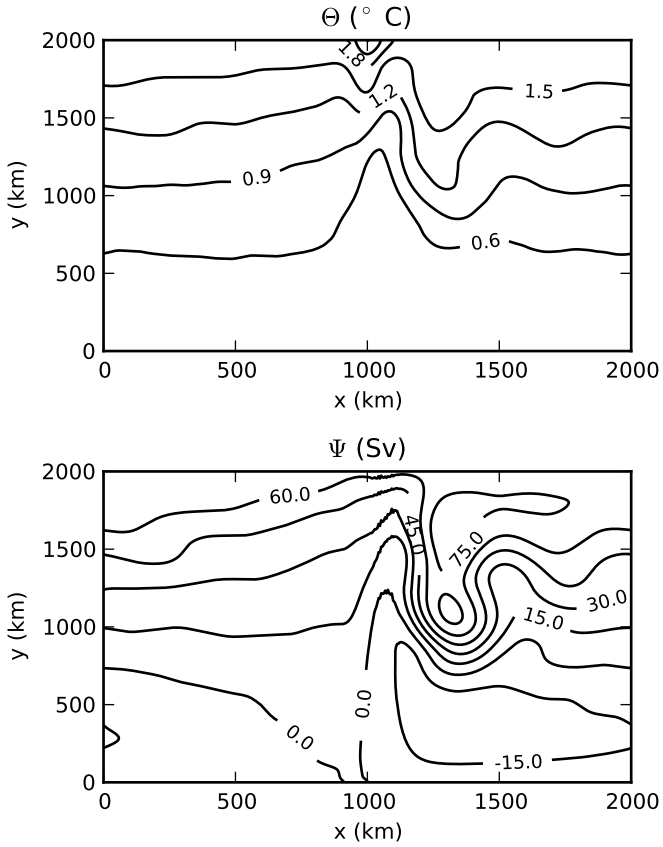

FIG. 7. The two streamwise coordinates Ψ and Θ, defined according to (20), for the reference ridge experiment ($\tau_0 = 0.2$ N m^{-2}).

where $\boldsymbol{v}_a$ and $\boldsymbol{v}_g$ are the ageostrophic and geostrophic components of the time-mean flow. The second term is the standing eddy flux and the third is the transient eddy flux (which is predominantly geostrophic). By decomposing the flux in this way, we can separately diagnose $\mathcal{H}^S_{Ek}$ (the ageostrophic, Ekman driven heat transport), $\mathcal{H}^S_g$ (the total geostrophic flow heat transport), $\mathcal{H}^S_{SE}$ (the standing-eddy component of $\mathcal{H}^S_g$), and $\mathcal{H}^S_{TE}$ (the transient-eddy component) using (19), analogously to the meridional heat transport components defined in Sec. 4. The difference is that these fluxes are across streamlines defined by S, rather than latitude circles. (By choosing $S = y$, we could recover the standard meridional heat transport definition.)

We examine these different components of the heat flux across Θ and Ψ contours in Fig. 8 for the reference simulations. (It is especially useful to compare with Fig. 4 from Sec. 4, showing the components of the heat flux across latitude circles.) We see that the overall magnitude of the cross-stream heat flux by the Ekman transport is similar in any coordinate system, peakings around 100 TW. This heat transport is balanced by a geostrophic flux, leading to very small net $\mathcal{H}^S$. However, by decomposing $\mathcal{H}^S_g$, the poleward heat transport by the geostrophic motions, into standing and transient components, we see that in either streamwise coordinate, *the standing eddy heat flux is indeed very close to zero*, and the transient eddies are what balance the Ekman-induced heat flux. This is in strong contrast to Fig. 4, where standing eddies dominated the flux across latitude circles.

We now examine how the balance depends on wind stress. The components of the heat transport across the Θ contour whose average latitude is $y = 1250$ km is shown in Fig. 9 for both flat and ridge experiments. (The equivalent results for Ψ are almost identical and are not shown.) In both cases, the increasing winds drive more and more heat across the Θ contours via the Ekman transport. In the flat experiments, of course only transient eddies can balance the increasing Ekman-induced heat flux across Θ contours, as with the meridional heat transport (Fig. 5) in the previous section. However, in the ridge case, the standing eddy component $\mathcal{H}^\Theta_{SE}$ remains rather small, in strong contrast to Fig. 5. Instead, like in the flat-bottomed experiments, the transient eddy heat flux is what primarily balances $\mathcal{H}^\Theta_{Ek}$ in the ridge case. We do point out that $\mathcal{H}^\Theta_{SE}$ is not negligible in the balance, achieving a value of about one third of $\mathcal{H}^\Theta_{TE}$ for the strongest winds. As suggested by Fig. 8, this is somewhat dependent on the particular Θ contour chosen. At different values of Θ, the relative importance of $\mathcal{H}^\Theta_{SE}$ is less, or even reversed in sign.

The initial impression given by the streamwise analysis is in line the perspective advanced by Marshall and Radko (2003) and Olbers and Visbeck (2005): that adopting a streamwise coordinate renders the system with topography isomorphic to the zonally symmetric case with no topography, wherein the dominant balance is between Ekman advection and transient eddy fluxes. But this picture is not complete; for one thing, the bulk heat transport efficiency K_g is demonstrably higher with topography, regardless of the coordinate system used, meaning that the transient eddies are actually more efficient at moving heat across streamlines when topography is present. A related issue is that the eddy heat flux itself is not distributed uniformly along a streamwise contour, as in the flat-bottom case—instead it is highly localized downstream of the ridge. To properly explore this, we must look at the local eddy heat flux in the (x, y) plane.

b. Local Cross-Stream Heat Flux

We now wish to decompose the structure of $\overline{\boldsymbol{v}\theta} \cdot \hat{\boldsymbol{n}}$ locally, to see where heat is fluxed across streamlines. In the flat-bottom case, all the statistics are completely homogeneous in the x-direction, meaning that each component of the cross-stream heat flux (Ekman and transient eddy)

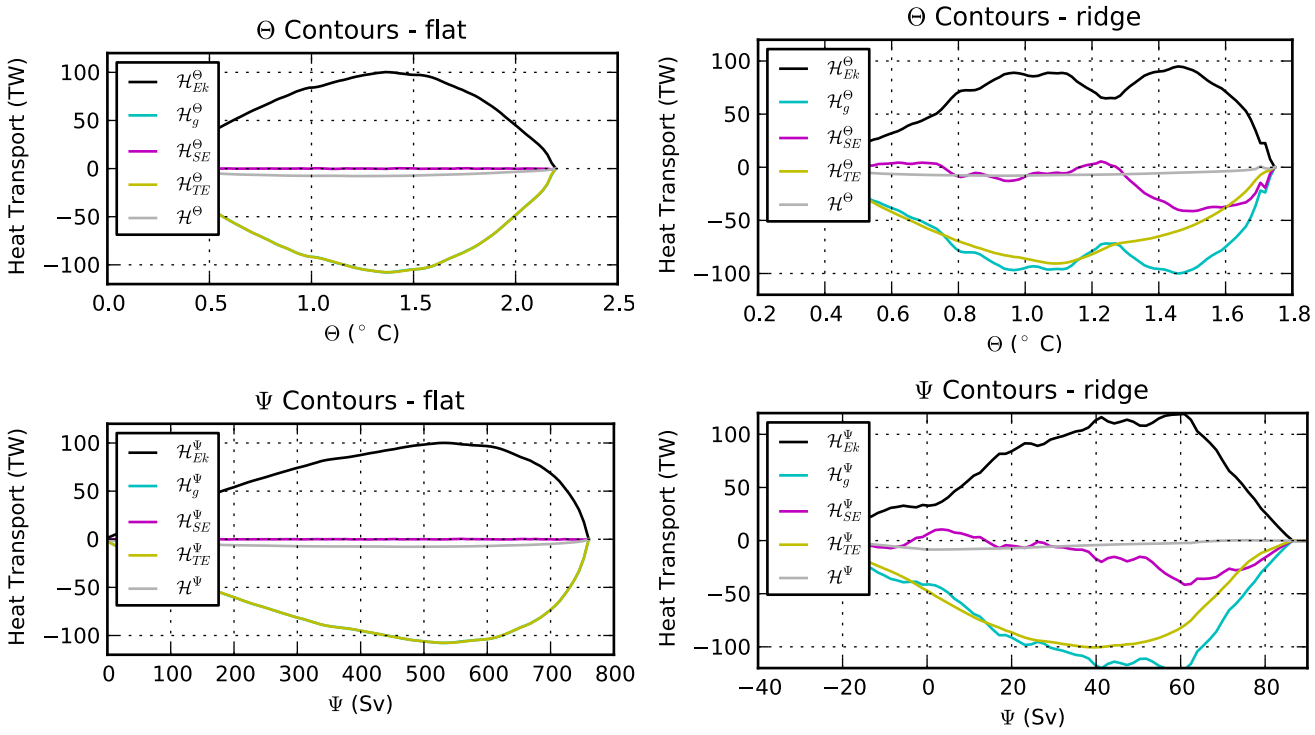

FIG. 8. Components of the heat transport across Θ contours (top panels) and Ψ contours (bottom panels) for the reference experiments ($\tau_0 = 0.2$ N m^{-2}). The flat bottom experiments are on the left, and the ridge experiments are on the right. The components are: $\mathcal{H}_{Ek}$, black, the ageostrophic (primarily Ekman-induced) part; $\mathcal{H}_g$, cyan, the heat-transport by geostrophic motions; $\mathcal{H}_{SE}$, magenta, the standing eddy part of $\mathcal{H}_g$; $\mathcal{H}_{TE}$, yellow, the transient eddy part of $\mathcal{H}_g$; and $\mathcal{H}$, light gray, the net heat flux across the contour.

is spread evenly along a streamline. Prior studies of idealized circumpolar currents with topographic ridges (**??**) have shown that eddy thickness fluxes (related to the PV flux) are concentrated in regions near and downstream of the topographic ridge. A similar conclusion was reached by **?** in an analysis of altimetric data; they found that Lagrangian trajectories cross the ACC fronts preferentially in a few locations downstream of major topographic features such as Drake Passage or Kerguelen plateau. Therefore, we should expect our eddy heat flux to be similarly localized.

To examine the local heat flux, first we note that, from (19), only the *divergent* part of $\overline{\boldsymbol{v}\theta}$ participates in the cross-stream heat flux. Yet locally, the eddy flux can be dominated by a rotational component, obscuring the physics of cross-stream transport (Marshall and Shutts 1981; **?**; **?**; **?**). In our numerical model, we can easily isolate the divergent part by solving the elliptic Poisson problem

$$\nabla^2\phi(x,y) = \nabla\cdot\left(\int_{-H}^{0}\overline{\boldsymbol{v}\theta}dz\right) \tag{22}$$

subject to the Neumann boundary condition that $\phi_x = 0$ at the northern and southern boundaries. The divergent component of the temperature flux is then given by

$$\boldsymbol{F}^{div}(x,y) = \nabla\phi\ . \tag{23}$$

We solve (22) for ψ numerically using an algebraic multigrid solver.[2] We also solve separately for the steady ageostrophic, geostrophic, and transient eddy components of the divergence, giving three separate fields $\boldsymbol{F}_a^{div}$, $\boldsymbol{F}_g^{div}$ and $\boldsymbol{F}_{TE}^{div}$. Dotted with $\hat{\boldsymbol{n}}$, these three components correspond with $\mathcal{H}_{Ek}^S$, $\mathcal{H}_{SE}^S$, and $\mathcal{H}_{TE}^S$, the three components of the cross-stream heat transport identified above.

These three components of the vertically integrated divergent eddy temperature flux ($\boldsymbol{F}_a^{div}$, $\boldsymbol{F}_g^{div}$ and $\boldsymbol{F}_{TE}^{div}$) are plotted in Fig. 10 as arrows in the (x,y) plane. This figure also shows the magnitude of the cross stream component of the flux. In this figure, Θ was used as the streamwise coordinate, and the Θ contours are also shown. We now discuss each component separately.

[2]This python-based solver is freely available at `https://code.google.com/p/pyamg/`.

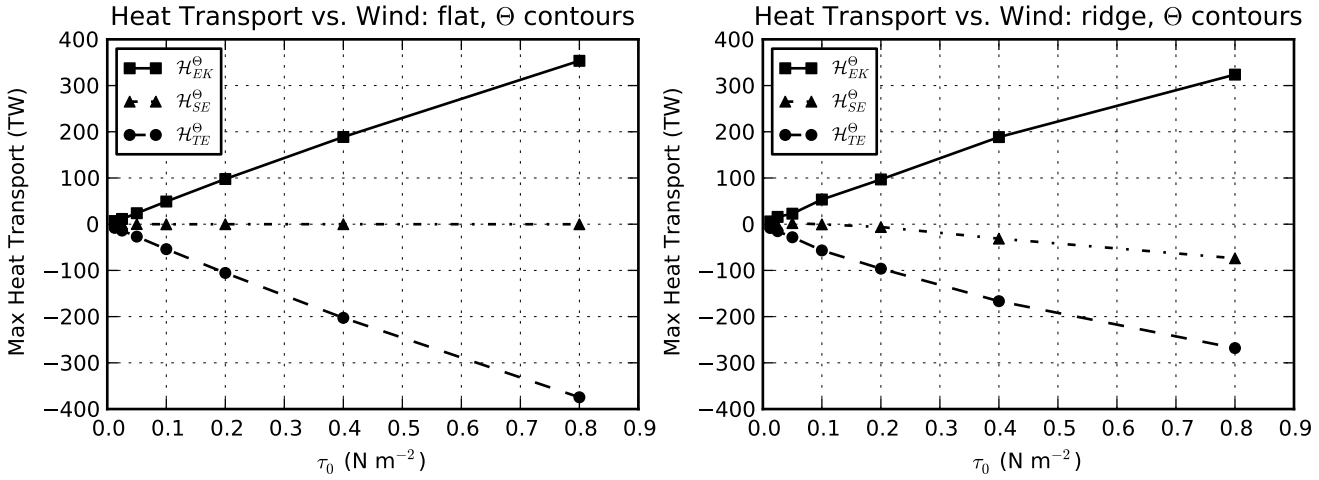

FIG. 9. The different components of the meridional heat transport across the Θ contour centered on $y = 1250$ km (where $\mathcal{H}_{Ek}$ is roughly maximum) for different values of the wind stress parameter τ_0. Otherwise similar to Fig. 5.

$\boldsymbol{F}_a^{div}$, the ageostrophic cross-stream flux, primarily illustrates the broad pattern of the Ekman transport bringing heat across the mostly-zonal Θ contours. However, in the vicinity of the standing-wave meander, the ageostrophic flux is not purely meridional. The zonal component cannot be due to Ekman transport, since the winds themselves are purely zonal. Instead it is caused by ageostrophic currents which are sustained by advective momentum transport. These dynamics are important locally but evidently not in an integral sense; as illustrated by Fig. 8, the magnitude of $\mathcal{H}^{\Theta}_{Ek}$ (which measures the net ageostophic flux across Θ contours) is quite close to that determined by Ekman transport alone.

The heat flux across streamlines from the steady, geostrophic flow is what we call $\boldsymbol{F}_{SE}^{div}$. According to Fig. 10, this flux carries heat locally in both directions across the Θ contours. The magnitude of this heat flux locally can be greater than the Ekman-induced flux, especially in the meander region. However, there is very little *net* heat flux across streamlines associated with this component. The positive and negative contributions along a Θ contour apparently cancel out, and $\mathcal{H}^{S}_{SE}$ integrates to nearly zero. This can be explained by the fact that that $\boldsymbol{F}_{SE}^{div}$ is almost completely due to advection of the vertically averaged temperature by the barotropic flow: i.e. $\nabla \cdot \boldsymbol{F}_{SE}^{div} \simeq J(\Psi, \Theta)$. (We checked this but did not plot it here.) It is obvious that an integral of such a flux across a contour of either Ψ or Θ must vanish identically. In the case of Ψ contours, this is because there can simply be no advection across the streamlines at all. In the case of Θ contours, it is because Θ is constant along the integration path and can be removed from the integral in (19), leaving only the barotropic transport, which also must integrate to zero across any closed contour. This vanishing of the barotropic flow contribution is what prompted de Szoeke and Levine (1981) to use Θ contours in their analysis. The remaining contribution to $\mathcal{H}^{\Theta}_{SE}$ is due to advection by the baroclinic mean flow. Evidently this contribution is small.

The most interesting and important part of Fig. 10 is $\boldsymbol{F}_{TE}^{div}$, the local divergent transient eddy heat flux across Θ contours. This eddy flux is what balances the positive flux of heat across Θ contours by the Ekman transport. The flux is nearly entirely down-gradient, as expected since it is just the divergent part (Marshall and Shutts 1981). What's more, the vectors of the divergent flux are aligned normal to the Θ contours, suggesting that these contours are indeed fundamental. (Recall that the method for identifying the divergent portion of the flux is completely unrelated to the choice of streamwise coordinates.) The cross-stream flux occurs mostly in the vicinity of the strong meander downstream of the ridge. In fact, close inspection of the arrows in Fig. 10 reveals that $\boldsymbol{F}_{TE}^{div}$ is mostly a *zonal* flux across the Θ contours running north-south. These zonal fluxes go in both direction out and away from the trough of the standing wave. No wonder the transient eddies did not make a strong contribution to the meridional heat transport! The most important eddy heat fluxes are actually zonal, not meridional at all.

From this divergent eddy heat flux, it is possible to construct a local cross-stream eddy diffusivity. We define this diffusivity as

$$K_{\perp}^{div}(x,y) = -\frac{1}{H}\frac{\boldsymbol{F}_{TE}^{div} \cdot \hat{\boldsymbol{n}}}{|\nabla\Theta|} \tag{24}$$

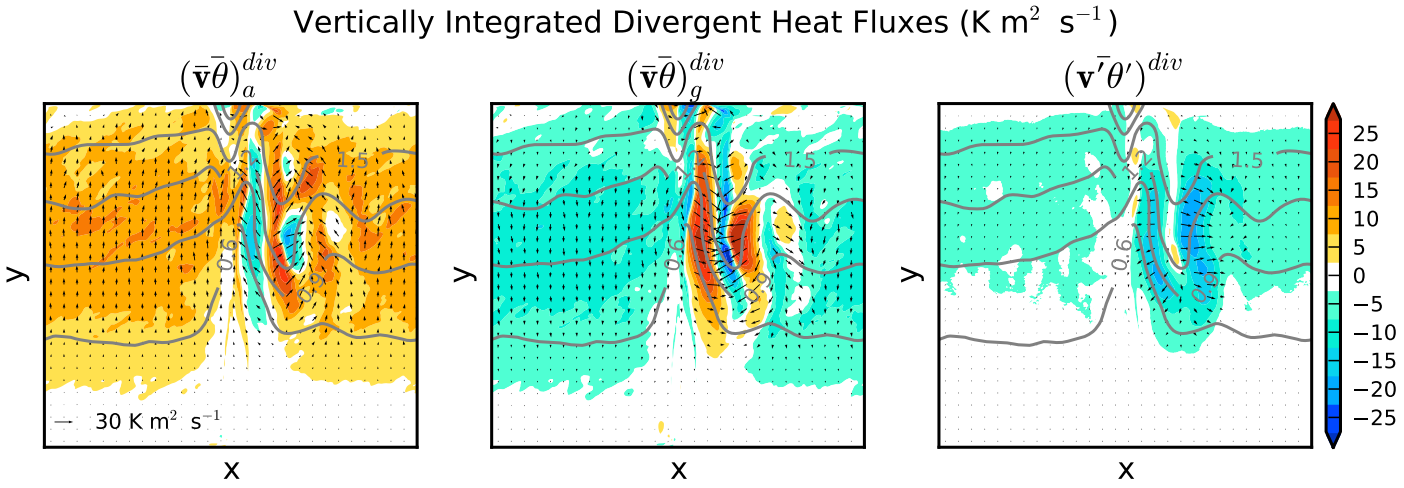

FIG. 10. *Top Row:* Components of the heat transport across Θ contours in the x, y plane.

where H is the full depth.[3] This quantity measures the local efficiency of eddies at transporting heat across the Θ contours. $K_\perp^{div}$ is plotted in Fig. 11, for both the flat and ridge reference experiments. For the flat-bottom experiment, $K_\perp^{div}$ is zonally uniform, peaking in the northern part of the domain around 4000 m^2 s^{-1}. For the ridge experiments, $K_\perp^{div}$ is highly variable in space. The region of highest diffusivity is is downstream of the ridge in the standing meander, particularly on the right side of the wave trough. In this region, diffusivities exceed 5000 m^2 s^{-1}. This region is precisely where the gradients are also strongest, leading to an extremely strong local cross-stream flux. In the western part of the domain, but the diffusivity and the gradient are weak. This local correlation between strong mixing and strong gradient is perhaps the greatest challenge for constructing a theoretical model based only on streamwise-averaged quantities. We will return to this point in the forthcoming discussion.

7. Discussion and Conclusions

[[I have started writing this section, but it is incomplete. Need to discuss more to decide what to emphasize.]]

We have examined the equilibration of idealized circumpolar currents with and without topography. The point of this exercise was to reach a deeper understanding of how the thermocline depth is determined. In our simplified problem, the thermocline depth is regulated completely by the efficiency of the geostrophic flow at transporting heat poleward. The amount of heat transported must approximately balance the equatorward heat transport by the Ekman circulation; the thickness of the layer over which the heat is returned poleward is the thermocline depth. A more efficient geostrophic heat transport can accomplish the necessary heat transport in a shallower layer.

We first analyzed the simulations using a standard zonal-averaged framework. From this perspective, the chief difference between the simulations with topography is that they contain both standing and transient eddies, while the flat-bottomed case contains only transient eddies. For the same forcing, the thermocline depth is significantly shallower when topography is present. Furthermore, the sensitivity of the thermocline depth to the wind stress is less when topography is present, indicating a more complete state of eddy saturation. In the experiments with topography, the geostrophic meridional heat transport is strongly dominated by the standing eddy contribution. Therefore, from this zonally averaged perspective, the eddy saturation phenomenon is properly understood as an equilibration between wind-driven Ekman fluxes and standing eddy fluxes. This should be kept in mind when analyzing more realistic models, where standing eddies play a similarly prominent role.

We also analyzed the heat transport across the the meandering front using two different "streamwise" coordinates, one based on the depth-averaged temperature (Θ) and one based on the barotropic transport streamfunction (Ψ).

Our study suggests that we have been framing the equi-

[3] Here we normalize $K_\perp^{div}$ by the full depth rather than just the thermocline depth, in contrast to the definition of K_g in (**??**). However, K_g is also defined based on the *surface* gradient $\partial\theta_s/\partial y$, rather than $\nabla\Theta$, the vertically-averaged gradient. Assuming that the zonal mean surface gradient is fixed, it can be shown that $\partial\Theta/\partial y \simeq (h/H)\partial\theta_s/\partial y$, i.e. that the depth-averaged gradient is proportional to the surface gradient scaled by the thermocline depth. Therefore, our two diffusivity definitions are consistent.

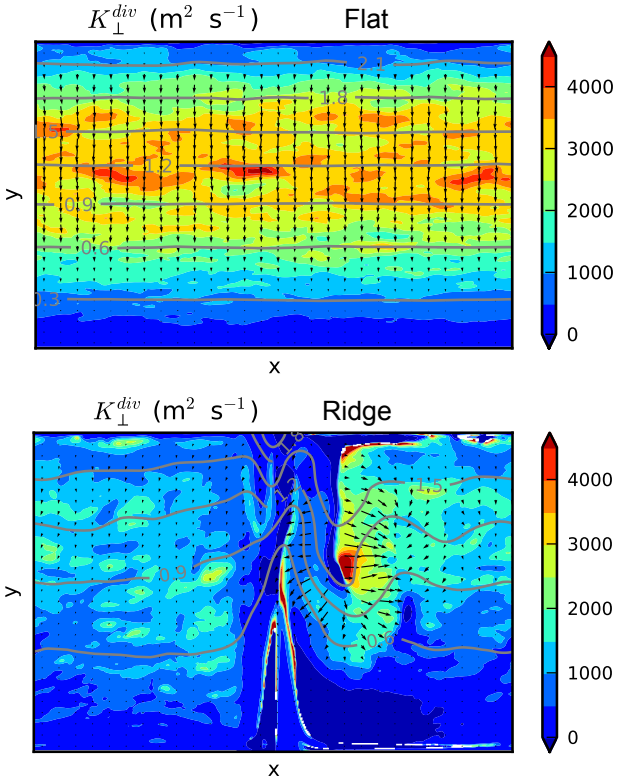

FIG. 11. Local eddy diffusivity for the vertically-integrated divergent eddy heat flux, defined according to (24). The Θ contours are shown in gray. The direction and magnitude of the divergent eddy heat flux $\boldsymbol{F}_{TE}^{div}$ are indicated by the black arrows. The integrated flux across contours is essentially the same in both experiments.

libration problem incorrectly. All of the current theoretical models for the ACC stratification rely on eddy diffusivity closures based on zonally or streamwise-averaged fields alone, i.e. a fundamentally axisymmetric background state (Johnson and Bryden 1989; Karsten et al. 2002; Cessi and Fantini 2004; Marshall and Radko 2003; Olbers and Visbeck 2005; Cessi 2008; Jansen and Ferrari 2012; Nikurashin and Vallis 2012). Many of these models can trace their closure schemes back to the two-layer quasigeostrophic equilibration problem studied by Held and Larichev (1996), or to the diffusive closures made by Green (1970) and Stone (1972) in an atmospheric context. (See also **?**Schneider 2006, for a review of the atmospheric side of the problem.) Ultimately, these theories are finite-amplitude, nonlinear closures of the classic baroclinic instability problems posed by Charney (1947), Eady (1949), and Phillips (1951) for zonally-symmetric background states.

A powerful criticism of this paradigm can be found in Pierrehumbert (1984), who examined the baroclinic instability of a simple flow with variations of the shear in the zonal direction. Such a problem is clearly applicable to our model, and indeed to the real ACC. There are important qualitative differences between this "local" instability problem and the classical zonally symmetric problem, such as a strong dependence on the barotropic zonal mean flow. (The zonally symmetric problem is essentially gallilean-invariant and is therefore insensitive to the addition of a barotropic mean zonal flow, but this invariance is broken by the addition of fixed topography.) The unstable local modes are confined spatially to the region downstream of the maximum shear.

The strong spatial variation in mixing along a Θ contour means that a diffusive closure for the cross-stream transient eddy heat flux based on the *streamwise-averaged* background gradient is unlikely to be satisfactory. To see this more clearly we can rewrite the cross-stream eddy heat transport using the diffusivity defined in (24) as

$$\mathcal{H}_{TE}^{\Theta} = \rho_0 c_p \oint_\Theta \boldsymbol{F}_{TE}^{div} \cdot \hat{\boldsymbol{n}} ds = -\rho_0 c_p \oint_\Theta K_\perp^{div} |\nabla\Theta| ds \ . \quad (25)$$

If $K_\perp^{div}$ were approximately constant along the contour, it could be removed from the integral, and $\mathcal{H}_{TE}^{\Theta}$ could be written only in terms of this constant and the streamwise-averaged $|\nabla\Theta|$. But in fact, Fig. 11 shows that $K_\perp^{div}$ and $|\nabla\Theta|$ are strongly correlated in space, with large diffusivity precisely where the gradients are strong.

Acknowledgments.

Start acknowledgments here.

APPENDIX

Is there one?

I don't know.

REFERENCES

Abernathey, R., J. Marshall, and D. Ferreira, 2011: The dependence of southern ocean meridional overturning on wind stress. *J. Phys. Oceanogr.*, **41 (12)**, 2261–2278.

Cenedese, C., J. Marshall, and J. A. Whitehead, 2004: A laboratory model of thermocline depth and exchange fluxes across circumpolar fronts. *J. Phys. Oceanogr.*, **34**, 656–668.

Cessi, P., 2007: Regimes of thermocline scaling: The interaction of wind stress and surface buoyancy. *J. Phys. Oceanogr.*, **37**, 2009–2021.

Cessi, P., 2008: An energy-constrained parameterization of eddy buoyancy flux. *J. Phys. Oceanogr.*, **38**, 1807–1820.

Cessi, P. and M. Fantini, 2004: The eddy-driven thermocline. *J. Phys. Oceanogr.*, **34**, 2642–2659.

Charney, J. G., 1947: The dynamics of long waves in a baroclinic westerly current. *J. Meteor.*, **4**, 135–162.

de Szoeke, R. A. and M. D. Levine, 1981: The advective flux of heat by mean geostrophic motions in the southern ocean. *Deep Sea Res.*, **28A (10)**, 1057–1085.

Dufour, C. O., J. Le Sommer, J. D. Zika, M. Gehlen, J. C. Orr, P. Mathiot, and B. Barnier, 2012: Standing and transient eddies in the response of the Southern Ocean meridional overturning to the Southern Annular Mode. *J. Climate*, **25**, 6958–6974.

Eady, E., 1949: Long waves and cyclone waves. *Tellus*, **1**, 33–52.

Farneti, R., T. L. Delworth, A. J. Rosati, S. M. Griffies, and F. Zeng, 2010: The role of mesoscale eddies in the rectification of the southern ocean response to climate change. *J. Phys. Oceanogr.*, **40**, 1539–1558.

Green, J. S. A., 1970: Transfer properties of the large-scale eddies and the general circulation of the atmosphere. *Quart. J. Roy. Meteor. Soc.*, **96**, 157–185.

Hallberg, R. and A. Gnanadesikan, 2006: The role of eddies in determining the structure and response of the wind-driven southern hemisphere overturning: Results from the modeling eddies in the souther ocean (meso) project. *J. Phys. Oceanogr.*, **36**, 2232–2252.

Haney, R. L., 1971: Surface thermal boundary condition for ocean circulation models. *J. Phys. Oceanogr.*, **1**, 241–248.

Held, I. M. and V. D. Larichev, 1996: A scaling theory for horizontally homogeneous, baroclinically unstable flow on a beta plane. *J. Atmos. Sci.*, **53 (7)**, 946–953.

Hill, C., D. Ferreira, J.-M. Campin, J. Marshall, R. Abernathey, and N. Barrier, 2012: Controlling spurios diapycnal mixing in eddy-resolving height-coordinate ocean models: Insights from virtual deliberate tracer release experiments. *Ocean Modelling*, **45-46**, 14–26.

Hughes, C. W., 1997: Comments on on the obscurantist physics of 'form drag' in theorizing about the circumpolar current. *J. Phys. Oceanogr.*, **27**, 209–210.

Jansen, M. and R. Ferrari, 2012: Macroturbulent equilibration in a thermally forced primitive equation system. *J. Atmos. Sci.*

Johnson, G. C. and H. L. Bryden, 1989: On the size of the Antarctic Circumpolar Current. *Deep Sea Res.*, **36**, 39–53.

Karoly, D. J., P. C. McIntosh, P. Berrisford, T. J. McDougall, and A. C. Hirst, 1997: Similarities of the deacon cell in the southern ocean and ferrel cells in the atmosphere cells in the atmosphere. *Q. J. R. Meteorol. Soc.*, **123**, 519–526.

Karsten, R., H. Jones, and J. Marshall, 2002: The role of eddy transfer in setting the stratification and transport of a circumpolar current. *J. Phys. Oceanogr.*, **32**, 39–54.

Karsten, R. and J. Marshall, 2002: Constructing the residual circulation of the acc from observations. *J. Phys. Oceanogr.*, **32**, 3315–3272.

Kuo, A., R. A. Plumb, and J. Marshall, 2005: Transformed eulerian-mean theory. part ii: Potential vorticity homogenization and equilibrium of a wind- and buoyancy-driven zonal flow. *J. Phys. Oceanogr.*, **45**, 175–187.

Large, W. G., J. C. McWilliams, and S. C. Doney, 1994: Oceanic vertical mixing: A review and a model with a nonlocal boundary layer parameterization. *Reviews of Geophysics*, **32 (4)**, 363–403.

Lee, M.-M. and A. Coward, 2003: Eddy mass transport for the Southern Ocean in an eddy-permitting global ocean model. *Ocean Modeling*, **5**, 249–266.

Marshall, G., 2003: Trends in the southern annular mode from observations and reanalyses. *J. Climate*, **16**, 4134–4144.

Marshall, J., A. Adcroft, C. Hill, L. Perelman, and C. Heisey, 1997a: A finite-volume, incompressible navier stokes model for studies of the ocean on parallel computers. *J. Geophys. Res.*, **102**, 5753–5766.

Marshall, J., C. Hill, L. Perelman, and A. Adcroft, 1997b: Hydrostatic, quasi-hystrostatic, and non-hydrostatic ocean modeling. *J. Geophys. Res.*, **102**, 5733–5752.

Marshall, J., H. Jones, R. Karsten, and R. Wardle, 2002: Can eddies set ocean stratification? *J. Phys. Oceanogr.*, **32**, 26–38.

Marshall, J., D. Olbers, H. Ross, and D. Wolf-Gladrow, 1993: Potential vorticity constraints on the dynamics and hydrography of the southern ocean. *J. Phys. Oceanogr.*, **23**, 465–487.

Marshall, J. and T. Radko, 2003: Residual mean solutions for the antarctic circumpolar current and its associated overturning circulation. *J. Phys. Oceanogr.*, **33**, 2341–2354.

Marshall, J. and G. Shutts, 1981: A note on rotational and divergent eddy fluxes. *J. Phys. Oceanogr.*, **21**, 1677–1681.

Meredith, M. P. and A. M. Hogg, 2006: Circumpolar response of southern ocean eddy activity to a change in the southern annular mode. *Geophys. Res. Lett.*, **33**, L16 608.

Meredith, M. P., A. C. Naveira Garabato, A. M. Hogg, and R. Farneti, 2012: Sensitivity of the overturning circulation in the southern ocean to decadal changes in wind forcing. *J. Phys. Oceanogr.*, **42**, 99–110.

Morrison, A. K. and A. M. Hogg, 2012: On the relationship between Southern Ocean overturning and acc transport. *J. Phys. Oceanogr.*

Munday, D., H. L. Johnson, and D. P. Marshall, 2012: Eddy saturation of equilibrated circumpolar currents. *J. Phys. Oceanogr.*

Nikurashin, M. and G. Vallis, 2012: A theory of the interhemispheric meridional overturning circulation and associated stratification. *J. Phys. Oceanogr.*

Olbers, D., 1998: Comments on "on the obscurantist physics of 'form drag' in theorizing about the circumpolar current". *J. Phys. Oceanogr.*, **28**, 1647–1655.

Olbers, D., D. Borowski, C. Voelker, and J. Wolff, 2004: The dynamical balance, transport and circulation of the antarctic circumpolar current. *Antarctic Science*, **16**, 439–470.

Olbers, D. and V. O. Ivchenko, 2001: On the meridional circulation and balance of momentum in the southern ocean of pop. *Ocean Dynamics*, **52**, 79–93.

Olbers, D. and M. Visbeck, 2005: A model of the zonally averaged stratification and overtuning in the souther ocean. *J. Phys. Oceanogr.*, **35**, 1190–1206.

Phillips, N. A., 1951: A simple three-dimensional model for the study of large-scale extratropical flow paterns. *J. Meteorology*, **8 (381-393)**.

Pierrehumbert, R. T., 1984: Local and global baroclinic instability of zonally varying flow. *J. Atmos. Sci.*, **41 (14)**, 2141–2163.

Prather, M. J., 1986: Numerical advection by conservation of second-order moments. *J. Geophys. Res.*, **91 (D6)**, 6671–6681.

Schneider, T., 2006: The general circulation of the atmosphere. *Annu. Rev. Earth Planet. Sci.*, **34**, 655–88.

Speer, K., S. Rintoul, and B. Sloyan, 2000: The diabatic deacon cell. *J. Phys. Oceanogr.*, **30**, 3212–3223.

Spence, P., O. A. Saenko, M. Eby, and A. J. Weaver, 2009: The southern ocean overturning: Parameterized versus permitted eddies. *J. Phys. Oceanogr.*, **39**, 1634–1652.

Stone, P. H., 1972: A simplified radiative-dynamical model for the static stability of rotating atmospheres. *J. Atmos. Sci.*, **29 (3)**, 405–417.

Straub, D., 1993: On the transport and angular momentum balance of channel models of the antarctic circumpolar current. *J. Phys. Oceanogr.*, **23 (776-783)**.

Thompson, A. F., 2010: Jet formation and evolution in baroclinic turbulence with simple topography. *J. Phys. Oceanogr.*, **40**, 257–274.

Toggweiler, J. R., 2009: Shifting westerlies. *Science*, **232**, 1434–1435.

Toggweiler, R. and J. Russell, 2008: Ocean circulation in a warming climate. *Nature*, **451**, 286–288.

Toggweiler, R. and B. Samuels, 1995: Effect of Drake Passage on the global thermohaline circulation. *Deep Sea Res. I*, **42 (4)**, 477–500.

Viebahn, J. and C. Eden, 2010: Toward the impact of eddies on the response of the southern ocean to climate change. *Ocean Modelling*, **34**, 150–165.

Viebahn, J. and C. Eden, 2012: Standing eddies in the meridional overturning circulation. *J. Phys. Oceanogr.*, **42**, 1486–1508.

Wolfe, C. L. and P. Cessi, 2010: What sets the strength of the mid-depth stratification and overturning circulation in eddying ocean models? *J. Phys. Oceanogr.*, **40**, 1520–1538.